INTERNATIONAL JOURNAL FOR NUMERICAL METHODS IN FLUIDS, VOL. 9, 713–730 (1989)

# COUPLED HEAT TRANSFER AND VISCOUS FLOW, AND MAGNETIC EFFECTS IN WELD POOL ANALYSIS

R. McLAY AND G. F. CAREY
*The University of Texas at Austin, Austin, TX 78712, U. S. A*

## SUMMARY

A finite element formulation and analysis is developed to study coupled heat transfer and viscous flow in a weld pool. The thermal effects generate not only buoyancy forces but also a variation in the surface tension which acts to drive the viscous flow in the molten weld pool. A moving phase boundary separates molten and solid material. Numerical experiments reveal the nature of the highly convective flow in the weld pool and the associated thermal profiles. The relative importance of buoyancy, surface tension, phase change, convection, etc. are examined. We also consider the sensitivity of the solution to the finite element mesh and related non-linear numerical instabilities. Of particular interest is the coupling of the thermal and viscous flow fields for the case when radial flow is inward or outward.

KEY WORDS Viscous flow Heat transfer Phase change Finite elements Magnetic field

## INTRODUCTION

A detailed knowledge of the temperature field and thermally induced flow in a weld pool is important in understanding the phenomena and in development of improved welding techniques. Experimental measurements of the temperature and flow velocity are difficult even for surface flow description. In fact, introduction of materials for surface flow visualization into the weld pool has been observed in some instances to radically alter the flow pattern. Mathematical analysis and numerical simulation offer the possibility of avoiding such difficulties to provide a better qualitative and quantitative description of the coupled solution behaviour. Moreover, one can conduct parametric studies to assess the importance of the effects that influence the weld pool shape and hence improve the weld process.

Consider a molten weld pool resulting from an applied surface temperature or heat flux (Figure 1). The thermal gradients induce buoyancy forces in the weld pool which, together with surface tension, tend to cause fluid flow. Experimental studies indicate that for many welding problems the convective flow can be adequately modelled as a Newtonian fluid. The effect of buoyancy can be included as a distributed body force depending on temperature by means of the well known Boussinesq approximation.[1, 2]

Surface tension is known to vary with temperature and hence produces an additional thermally induced surface shear force (the Marangoni effect) during the flow (see e.g. References 3 and 4). Depending on the welding conditions and presence of impurities, the resulting shear force may be inwardly or outwardly directed. The exact nature of this process is not yet fully understood.[5] The velocity of the flow in the pool is sufficiently large that non-linear effects are significant. The

0271-2091/89/060713-18$09.00

*Received 21 April 1987*
*Revised 3 August 1988*

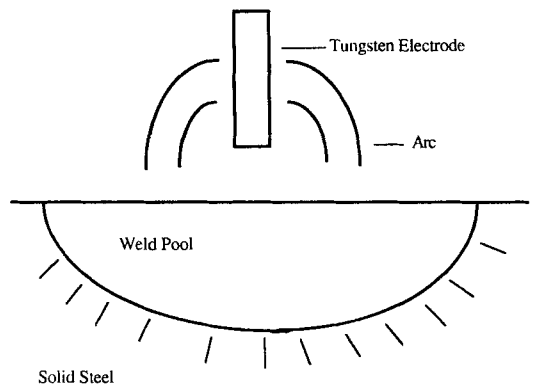


Figure 1. Sketch of the TIG welding system

strength and direction of the convective flow field will, in turn, influence the temperature field of the weld pool.

The problem is further complicated by the presence of a moving phase boundary between molten and solid material. Since the location of this phase boundary is not known *a priori*, this introduces an additional non-linearity to the problem.[6, 7] The influence of the convective flow on the temperature field in the weld pool will, in turn, affect the melt surface and hence the shape of the weld (see Reference 8 for a related physical problem, electron beam vaporization). Finally, in tungsten–inert gas (TIG) welding, electromagnetic effects generate body forces in the flow which may be significant in some situations (e.g. at high currents).

The problem may also be viewed as part of a larger problem when coupled to the heat transfer and flow in the plasma above the pool surface. This aspect is not considered here, and we assume that the surface temperature or heat flux is known (e.g. from experimental data).

In the present study we develop an integral statement and Galerkin finite element formulation of the coupled heat transfer and viscous flow problem including buoyancy, surface tension and the moving phase boundary. (For further discussion of finite elements for fluid flow and heat transfer, see e.g. References 9–14.) By means of detailed calculations using a fine mesh on a CRAY-XMP supercomputer, we seek to determine the detailed structure of the flow and temperature fields, including such features as primary and secondary circulations and layers. Such a precise description has not previously been obtained. Some exploratory finite difference studies are given in Reference 15. The effect of inward and outward driven flows on the size of the circulation patterns and the layer structure is of special interest, since this has a strong bearing on the shape of the weld pool.

## GOVERNING EQUATIONS

The transfer of heat in the weld pool is governed by

$$\rho c_p \frac{\partial T}{\partial t} + \rho c_p \mathbf{u} \cdot \nabla T - \nabla \cdot (k \nabla T) = 0, \tag{1}$$

where $c_p$ is the heat capacity, $k$ is the thermal conductivity, $T$ is the temperature and $\mathbf{u}$ is the velocity of the viscous flow. At the free surface the temperature distribution or heat flux is

prescribed; e.g. for an axisymmetric pool $T = T(r, 0, t)$ or $q(t) = -k(\partial T/\partial z)\ (r, 0, t)$ are given, where $r$ is the radial co-ordinate and $z = 0$ is the free surface (Figure 1). Since the problem is axisymmetric, we can consider the right quadrant alone with symmetry enforced on the vertical axis:

$$\frac{\partial T}{\partial r} = 0 \quad \text{on } r = 0. \tag{2}$$

The phase boundary moves with normal velocity $V$ satisfying the Stefan condition

$$[\![k \nabla T \cdot \mathbf{n}]\!] = LV \tag{3}$$

together with

$$T = T_{\text{melt}} \tag{4}$$

on the phase boundary, where $L$ is the latent heat coefficient for phase change of the material, $T_{\text{melt}}$ is the melting temperature and the notation $[\![\cdot]\!]$ denotes the flux jump.

This heat transfer problem is coupled to the viscous flow in the weld pool. Experimental studies have shown that, for the welding problems of interest, the surface flow velocities may reach magnitudes of order 1 m $s^{-1}$. For the length scale and viscosity of the weld pools considered, this implies a flow Reynolds number $Re$ of order 1000. Thus the assumption of linear Stokes flow is not applicable, and we use the Navier–Stokes equations for viscous flow of an incompressible fluid. Introducing the well known Boussinesq approximation, the viscous flow equations are

$$\frac{\partial \mathbf{u}}{\partial t} + \mathbf{u} \cdot \nabla \mathbf{u} - \nu \nabla \mathbf{u} + \frac{1}{\rho} \nabla p = -\beta(T - T_0)\mathbf{g} + \mathbf{f}_m, \tag{5}$$

$$\nabla \cdot \mathbf{u} = 0, \tag{6}$$

where $\mathbf{u}$ is the velocity, $p$ is the pressure, $T$ is the temperature, $T_0$ is a reference temperature (at which buoyancy forces are zero), $\nu$ is the viscosity, $\rho$ is the density, $\beta$ is the coefficient of thermal expansion of the fluid, $\mathbf{g} = -g\mathbf{i}_z$ is the vertical force due to gravity, and $\mathbf{f}_m$ is the magnetic force $\mathbf{J} \times \mu_m \mathbf{H}$ for a field of magnetic intensity $\mathbf{H}$ due to current $\mathbf{J}$.

There is 'no slip' at the melt boundary (since there is no volume change during melting), hence

$$\mathbf{u} = \mathbf{0} \quad \text{on } \partial\Omega_m; \tag{7}$$

and from symmetry there is no flow normal to the axis:

$$u_r = 0 \quad \text{on } r = 0, \tag{8}$$

where $u_r$ is the radial velocity component. The applied temperature field induces a surface tension equivalent to the application of shear stress at the horizontal free surface:

$$\mu \frac{\partial u_r}{\partial z} = \frac{\partial \gamma}{\partial T} \frac{\partial T}{\partial r} \quad \text{on} \quad \partial\Omega_f, \tag{9}$$

where $\gamma(T)$ is the interfacial tension and is known from experiment.

The quasi-static Maxwell equations are introduced to determine the magnetic field. If the magnetic permeability $\mu_m$ is assumed constant and the electric current density vector has non-zero components in the $r$- and $z$-direction (implying that $H_r$ and $H_z$ are zero), then the magnetic field intensity $\mathbf{H} = H_\phi \mathbf{i}_\phi$ satisfies

$$\mu_m \left( \frac{\partial \mathbf{H}}{\partial t} + \mathbf{u} \cdot \nabla \mathbf{H} \right) = \frac{1}{\sigma} \Delta \mathbf{H}, \tag{10}$$

where $\sigma$ is the electrical conductivity.

Recall that $\mathbf{J} = \nabla \times \mathbf{H}$ so that, using Stokes theorem,

$$\oint_s \mathbf{H} \cdot \mathrm{d}\mathbf{s} = \int_A \mathbf{J} \cdot \mathbf{n} \, \mathrm{d}A. \tag{11}$$

Hence the associated boundary conditions for the magnetic field can be obtained from boundary conditions on **J**. In particular, zero radial current flow at the centre line applies from symmetry and there is no current flow through the bottom of the slab. That is,

$$J_r = 0 \quad \text{at} \quad r = 0, \qquad J_z = 0 \quad \text{at} \quad z = -d. \tag{12}$$

At the top surface the arc is assumed to provide a current profile in the form of a truncated Gaussian distribution for $r \leqslant R$. That is, at $z = 0$

$$J_z = \frac{I}{\pi r_j^2} e^{-r^2/r_j^2} \quad \text{for} \quad r \leqslant R, \tag{13}$$

where $I$ is the total current input and $r_j$ is the standard deviation for the arc distribution. On the boundary side $r = R$ the current density is uniform with

$$J_z = \frac{I}{2\pi r d}. \tag{14}$$

Using (12)–(14) in (11) yields the desired boundary conditions for $H$. Specifically,

$$H_\phi(r, 0) = \frac{I}{2\pi r}(1 - e^{-r^2/r_j^2}), \qquad H_\phi(R, z) = H_\phi(R, 0)\left(1 + \frac{z}{d}\right). \tag{15}$$

The above equations, together with intial data for **u**, $T$ and $H_\phi$, constitute the mathematical statement of the problem.

## INTEGRAL FORMULATION AND FINITE ELEMENT APPROXIMATION

A variational form for the coupled problem on a fixed domain can be constructed by introducing weighted residual projections for the governing partial differential equations and applying the divergence theorem in the standard manner.[16, 17] Then, for the coupled problem on a fixed domain, we have the weak statement: the solution ($\mathbf{u}$, $p$, $T$, $H_\phi$) satisfies

$$\int_\Omega \left( \frac{\partial \mathbf{u}}{\partial t} \cdot \mathbf{v} + \mathbf{u} \cdot \nabla \mathbf{u} \cdot \mathbf{v} + \nu \nabla \mathbf{u} : \nabla \mathbf{v} - \frac{p}{\rho} \nabla \cdot \mathbf{v} \right) \mathrm{d}x + \int_{\partial \Omega_f} \frac{\partial \gamma}{\partial T} \frac{\partial T}{\partial r} \mathbf{i}_r \cdot \mathbf{v} \, \mathrm{d}s$$

$$= \int_\Omega \{ -\beta (T - T_0) \mathbf{g} \cdot \mathbf{v} + \mathbf{f}_m \cdot \mathbf{v} \} \mathrm{d}x, \tag{16}$$

$$\int_\Omega q \nabla \cdot \mathbf{u} \, \mathrm{d}x = 0, \tag{17}$$

$$\int_\Omega \left( \rho c_p \frac{\partial T}{\partial t} w + \rho c_p \mathbf{u} \cdot \nabla T w + k \nabla T \cdot \nabla w \right) \mathrm{d}x = 0 \tag{18}$$

and

$$\int_\Omega \left( \mu_m \frac{\partial H_\phi}{\partial t} \bar{w} + \mu_m \mathbf{u} \cdot \nabla H_\phi \bar{w} + \frac{1}{\sigma} \nabla H_\phi \cdot \nabla \bar{w} + \frac{H_\phi \bar{w}}{\sigma r^2} \right) \mathrm{d}x = 0 \tag{19}$$

for all admissible test functions $\mathbf{v}$, $q$, $w$ and $\bar{w}$. Here $\nabla\mathbf{u}:\nabla\mathbf{v}$ is the dyadic product symbolic representation for

$$\sum_{i,j}\frac{\partial u_i}{\partial x_j}\frac{\partial v_i}{\partial x_j},$$

and $\mathbf{v}$, $w$ and $\bar{w}$ vanish on those parts of the boundary where $\mathbf{u}$, $T$ and $H_\phi$ respectively are specified as essential data. If the normal heat flux $Q$ is specified on $\partial\Omega_f$, then we have the additional boundary integral $\int_{\partial\Omega_f} Qw\,ds$ on the right in (18). Introducing a finite element discretization and basis yields the semidiscrete coupled finite element system to be integrated in time.

A corresponding variational statement for the moving boundary problem can be constructed directly as a variational inequality. However, the variational inequality formulation has generally proven most useful in deriving error estimates for problems with constraints and proving convergence, rather than developing algorithms.[18, 19] Here we are concerned with the approximate formulation and numerical treatment, including the moving boundary, so we turn now to this issue.

A direct approach is to uncouple the phase boundary motion from the flow and transport equations in a time step $\Delta t$. The method is most easily described for the one-phase Stefan problem in one dimension. Then (3) becomes

$$-k\frac{\partial T}{\partial x} = LV$$

or

$$V = -\frac{k}{L}\frac{\partial T}{\partial x}. \tag{20}$$

Let $s(t)$ denote the position of the phase boundary. Since $V = ds/dt$, integrating (20) numerically with respect to time through time step $\Delta t$, the forward Euler scheme implies (Figure 2)

$$s(t+\Delta t) = s(t) - \frac{k}{L}\frac{\partial T}{\partial x}(s(t), t)\,\Delta t, \tag{21}$$

where the flux has been approximated as constant through the step.

This strategy can be extended immediately to higher dimensions. The problem now is to solve the associated heat transfer and viscous flow equations through the time step $\Delta t$ and including the influence of the domain change. An analysis of a scheme based on this technique for advancing the front in the model heat conduction equation has been developed demonstrating convergence. The forward Euler method is used to integrate in time on the current subdomain and extrapolation used over the incremental domain extension. This scheme offers low accuracy but does

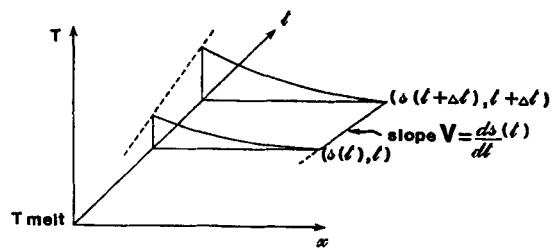


Figure 2. Movement of 1D phase boundary through a time step $\Delta t$

confirm that such strategies are viable for this class of problems. Higher-order predictor–corrector schemes for advancing the phase boundary can be formulated.

A more important issue is the problem of accurately solving the coupled flow and transport equations on the evolving domain. Transformation techniques may be introduced for adjusting the domain map and including the effect in the transformed governing equations. Both regular and space–time finite element approaches may be developed. Here we present one such method. This approach is a simplified approximation of the transformation procedure underlying moving finite element techniques.[15, 16]

Introducing the transformation $\mathbf{x} = \mathbf{x}(\xi, \tau)$, $t = \tau$, the time derivative in (1) transforms as

$$\frac{\partial T}{\partial t} = \frac{\partial T}{\partial \tau} - \sum_{i=1}^{N} \frac{\partial T}{\partial x_i}\frac{\partial x_i}{\partial \tau} = \frac{\partial T}{\partial \tau} - \mathbf{U}\cdot\nabla T, \tag{22}$$

where $\mathbf{U}$ is the transformation velocity. Thus we see that the effect of the transformation velocity enters as a convective adjustment $\mathbf{U}\cdot\nabla T$ to the governing equations. A similar expression applies for $\partial\mathbf{u}/\partial t$ in the viscous flow equation (5).

In particular, we are primarily concerned with the effect of the moving phase boundary. Let $\mathbf{V}$ be the velocity of the phase boundary at $\mathbf{x} = \mathbf{x}_s$. Then $\mathbf{V} = V_n\delta(\mathbf{x} - \mathbf{x}_s)\mathbf{n}$ since melting is in the direction normal to the interface $\mathbf{x} = \mathbf{x}_s$ at any time $\tau$. Setting $\mathbf{V}$ for $\mathbf{U}$ in (22) and substituting for $\partial\mathbf{u}/\partial t$ and $\partial T/\partial t$ in (5) and (1), then (16) and (18) become

$$\int_\Omega \left(\frac{\partial \mathbf{u}}{\partial \tau}\cdot\mathbf{v} - \mathbf{V}\cdot\nabla\mathbf{u}\cdot\mathbf{v} + \nu\Delta\mathbf{u}:\Delta\mathbf{v} - \frac{p}{\rho}\nabla\cdot\mathbf{v}\right)dx$$

$$= \int_\Omega \{-\beta(T - T_0)\mathbf{g}\cdot\mathbf{v} + \mathbf{f}_m\cdot\mathbf{v}\}dx - \int_{\partial\Omega_f} \frac{\partial\gamma}{\partial T}\frac{\partial T}{\partial r}\mathbf{i}_r\cdot\mathbf{v}\,ds \tag{23}$$

and

$$\int_\Omega \left\{\rho c_p\left(\frac{\partial T}{\partial \tau}w - \mathbf{V}\cdot\nabla T w\right) + \rho c_p\mathbf{u}\cdot\nabla T w + k\nabla T\cdot\nabla w\right\}dx = 0, \tag{24}$$

$$\int_\Omega \left\{\mu_m\left(\frac{\partial H_\phi}{\partial t}\bar{w} - \mathbf{V}\cdot\nabla H_\phi\bar{w}\right) + \mu_m\mathbf{u}\cdot\nabla H_\phi\bar{w} + \frac{1}{\sigma}\nabla H_\phi\cdot\nabla\bar{w} + \frac{H_\phi\bar{w}}{\sigma r^2}\right\}dx = 0 \tag{25}$$

for all admissible test functions $\mathbf{v}$, $w$ and $\bar{w}$ respectively.

Introducing the semidiscrete finite element expansions for $\mathbf{u}$, $p$, $T$ and $H_\phi$,

$$\mathbf{u}_h = \sum_{j=1}^{N} \mathbf{u}_j(\tau)\phi(\mathbf{x}),$$

$$p_h = \sum_{k=1}^{M} p_k(\tau)\chi_k(\mathbf{x}),$$

$$T_h = \sum_{l=1}^{L} T_l(\tau)\psi_l(\mathbf{x}),$$

$$H_h = \sum_{i=1}^{I} H_i\zeta_i(\mathbf{x}), \tag{26}$$

and $\mathbf{v}_h = \{(\phi_r, 0), (0, \phi_r)\}$ $q = \{\chi_s\}$, $w_h = \{\psi_t\}$ and $\bar{w}_h = \zeta_i$ into the integral statement (17), (23), (24), where $\{\phi_j, \chi_k, \psi_l, \zeta_i\}$ are the finite element basis functions on the discretized domain, yields the Galerkin approximate statement of the coupled problem. Evaluating element contributions to

the integrals so obtained and accumulating, we obtain a non-linear semidiscrete coupled system of ordinary differential equations

$$\mathbf{M}_1 \frac{\mathrm{d}\mathbf{u}}{\mathrm{d}t} + \mathbf{g}_1(\mathbf{u}, \mathbf{V}) + \mathbf{A}_1\mathbf{u} + \mathbf{B}\mathbf{p} = \mathbf{f}_1(\mathbf{T}, \gamma(\mathbf{T})),$$

$$\mathbf{B}^T\mathbf{u} = \mathbf{0},$$

$$\mathbf{M}_2 \frac{\mathrm{d}\mathbf{T}}{\mathrm{d}t} + \mathbf{g}_2(\mathbf{u}, \mathbf{V}, \mathbf{T}) + \mathbf{A}_2\mathbf{T} = \mathbf{f}_2,$$

$$\mathbf{M}_3 \frac{\mathrm{d}\mathbf{H}}{\mathrm{d}t} + \mathbf{g}_3(\mathbf{u}, \mathbf{V}, \mathbf{H}) + \mathbf{A}_3\mathbf{H} = \mathbf{f}_3 \tag{27}$$

to be integrated with respect to time.

In a given (small) time step $\Delta t$ from $t_n$ to $t_{n+1} = t_n + \Delta t$ we use the solution $\mathbf{u}^{(n)}$, $p^{(n)}$, $T^{(n)}$ at the beginning of the step to define $\mathbf{V}(t)$ from (3), and $\mathbf{V}$ in (27) is assumed constant through the step. Hence the convective adjustment term associated with the motion of the domain boundary is constant in a given time step, with value dependent upon $\mathbf{V}_n$, computed from the previous step. Differencing (27) implicitly with respect to time through the time step $\Delta t_n$ then yields a coupled non-linear system of algebraic equations to be solved for the nodal solution vector $(\mathbf{u}_r, \mathbf{u}_z, \mathbf{p}, \mathbf{H})$. In the present numerical algorithm we first iteratively decouple the energy and momentum equations in (27) by successive approximation of $\mathbf{T}$ and $\mathbf{u}$ respectively, with initial iterates given by the solution at the previous step. That is, through a given time step $(t_n, t_{n+1})$ we integrate with the decoupling iteration for $k = 0, 1, 2 \ldots$

$$\mathbf{M}_1 \frac{\mathrm{d}\mathbf{u}}{\mathrm{d}t} + \mathbf{g}_1(\mathbf{u}, \mathbf{V}_n) + \mathbf{A}_1\mathbf{u} + \mathbf{B}\mathbf{p} = \mathbf{f}_1(\mathbf{T}^{(k)}, \gamma(\mathbf{T}^{(k)})), \tag{28}$$

$$\mathbf{B}^T\mathbf{u} = \mathbf{0}, \tag{29}$$

$$\mathbf{M}_2 \frac{\mathrm{d}\mathbf{T}}{\mathrm{d}t} + \mathbf{g}_2(\mathbf{u}^{(k+1)}, \mathbf{V}_n, \mathbf{T}) + \mathbf{A}_2\mathbf{T} = \mathbf{f}_2, \tag{30}$$

$$\mathbf{M}_3 \frac{\mathrm{d}\mathbf{H}}{\mathrm{d}t} + \mathbf{g}_3(\mathbf{u}^{(k+1)}, \mathbf{V}_n, \mathbf{H}) + \mathbf{A}_3\mathbf{H} = \mathbf{f}_3. \tag{31}$$

Successive approximation and Newton–Raphson iterations have been implemented for (28), (29) with frontal elimination of the resulting linear systems and also for the linear systems arising from (30) and (31). The number of iterations can be varied according to the size of time step. In the numerical studies following, we use a backward Euler implicit scheme to interate (28), (30) and (31) with time step $\Delta t$ related to the specified surface temperature $T(r, 0, t)$ or flux $q(r, 0, t)$. The magnetic field calculation is also decoupled and the resulting algebraic system is solved using an element-by-element vectorized conjugate gradient algorithm.[20] Note that in this study we have used a standard Galerkin formulation. Since we observed that convection is not negligible in weld pool flows, some caution must be exercised with regard to grid size to ensure that the cell Reynolds and cell Peclet values are sufficiently small for oscillations not to occur. An alternative is to add artificial or numerical dissipation (via upwinding). In the present case the flow develops strong convective rolls so (streamline) directional upwinding may be applicable but is probably still not appropriate. Our purpose in this study is to obtain a detailed accurate solution to better delineate layers and recirculation zones. With this in mind, and since the convective effects are of

reasonable magnitude, we use a standard Galerkin scheme on a sufficiently fine mesh and do not add dissipation.

The eight-node serendipity element has been used in these calculations. In a previous numerical study[21] we showed that this element produces good velocities but inaccurate pressure on coarse discretizations for driven cavity type flows. The poor pressure approximation is due to the corner singularity and the incompressibility constraint. Results on moderate and fine grids are good and can be improved further by regularizing the boundary data at the singular point.

Note that this is only an approximate and simplified form of the continuously deforming finite element method in References 22 and 23. In the present method, only the nodes on the phase boundary move, other nodes remaining fixed. This implies that the elements adjacent to the phase boundary become increasingly elongated as time progresses. There are two main ways to circumvent this: (1) allow all nodes to move in the manner of the continuously deforming finite element method; (2) periodically redistribute the mesh (remesh). In the former approach the problem is solved for the solution and mesh co-ordinates simultaneously, thereby increasing the number of unknowns and size of the system significantly. Remeshing essentially uncouples the grid motion. To continue the solution we compute the change in mesh location over the time step and determine a mesh velocity $\mathbf{V}$ for use in (28)–(31). In the present analysis we have adopted a remesh strategy based on the procedures developed in Reference 24. The motion of the phase boundary determined by $\mathbf{V} \cdot \mathbf{n}\, \Delta t$ is used to interpolate the motion of interior nodes and adjust the grid accordingly.

## NUMERICAL RESULTS

To investigate the nature of the convective flow and relative influence of buoyancy and surface tension, we first considered a fixed domain problem integrated to a steady state, i.e. we considered the problem for a molten pool held in a crucible with specified final surface temperature and melt temperature maintained at the crucible. The domain shape was chosen to approximate that obtained in experiments and used previously in finite difference computations in Reference 15. An eight-node quadratic $C^0$ basis for the velocity and temperature with a bilinear $C^0$ pressure basis is used in our extension of the implementation in Reference 11.

The physical properties for molten steel in the weld pool problem are: coefficient of expansion $\beta = 10^{-4}\ \mathrm{K}^{-1}$; thermal conductivity $k = 40\ \mathrm{W\,mK}^{-1}$; density $\rho = 7200\ \mathrm{kg\,m}^{-3}$; heat capacity $c_p = 753\ \mathrm{J\ kg}^{-1}\ \mathrm{K}^{-1}$; kinematic viscosity $\nu = 8{\cdot}33 \times 10^{-7}\ \mathrm{m}^2\,\mathrm{s}^{-1}$. The corresponding Prandtl number for the weld pool is 0·113. The temperature boundary condition at the surface in the following numerical experiments has been specified as

$$T(r, 0) = \tfrac{1}{2}(T_{\max} - T_{\mathrm{melt}}) \cos(\pi r/R) + \tfrac{1}{2}(T_{\max} + T_{\mathrm{melt}}),$$

where $T_{\mathrm{melt}} = 1600$ K, $R$ is the maximum radial distance, and the maximum temperature $T_{\max}$ is known from experimental data.[25,26]

Setting surface tension to zero, we first considered the flow field produced by buoyancy alone and obtained the velocity field in Figure 3. (Velocity vectors for the weld pool flow are scaled in the plots so that in each case the scaled maximum velocity is unity.) We find that the flow velocity generated by buoyancy is small. The maximum velocity occurs at the surface and is approximately 0·005 $\mathrm{m\,s}^{-1}$. Hence the problem is only mildly non-linear and solution was obtained in a few successive approximation iterations. It is clear that the contribution of buoyancy is negligible for the weld pool circulatory flows. An order of magnitude and perturbation analysis can also be constructed to arrive at this qualitative conclusion. The Lorentz body force $\mathbf{J} \times \mu_{\mathrm{m}}\mathbf{H}$ also

influences the velocity field. To examine this contribution we again set the surface tension to zero and also now omit the buoyancy force. The velocity field resulting for a magnetic field due to a current $I = 100$ A is shown in Figure 4. The Lorentz force causes an inwardly directed flow but the maximum velocity is only 0·02 m s$^{-1}$. If the electric current is increased to 200 A, the velocity field is similar with a maximum velocity now of 0·063 m s$^{-1}$ (see also Reference 27).

Next we considered the surface tension driven problem at increasing Reynolds numbers *Re*. Rather than solve the steady problem with continuation in *Re*, we take the transient problem with the surface data incrementally increasing from zero to the desired value as indicated in the previous discussion of implementation. In the following calculations the horizontal component of the surface flow velocity was prescribed using $\gamma(T)$ and $\partial T/\partial r$ at $z = 0$. The surface tension coefficient is assumed to vary linearly. The slope $\partial\gamma/\partial T$ used for each calculation is given in the figures. A successful solution on a coarse mesh of 100 elements (Figure 5) was obtained for moderate *Re*, but the method failed to converge at $Re \sim 1200$ for this mesh. Local solution oscillations feed back into the non-linear terms of the equations, and the solution iterates diverge. On uniformly refining the mesh to 200 elements, a convergent solution was obtained, and a mesh of 450 elements produced essentially the same flow pattern (Figure 6). There is a strong circulatory flow at the extreme right of the domain and a flow reversal in the boundary layer adjacent to the free surface. Elsewhere in the flow field the velocities are small (although a streamline plot does indicate a mild secondary circulation).

The associated temperature contours are shown in Figure 7 and are compared with the temperature contours for conduction in the absence of convection (which would also be close to

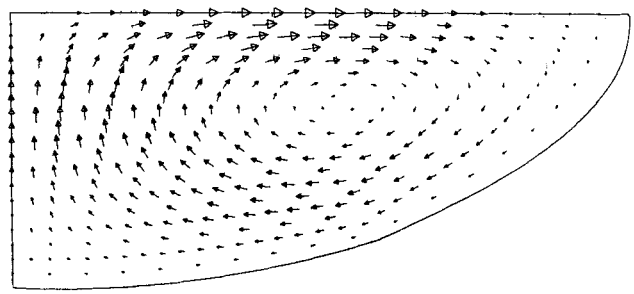

Figure 3. Velocity field for flow in a fixed axisymmetric domain due to buoyancy forces; $V_{max} = 4{\cdot}3$ mm s$^{-1}$, $Pr = 0{\cdot}11$, $Ra = 430$

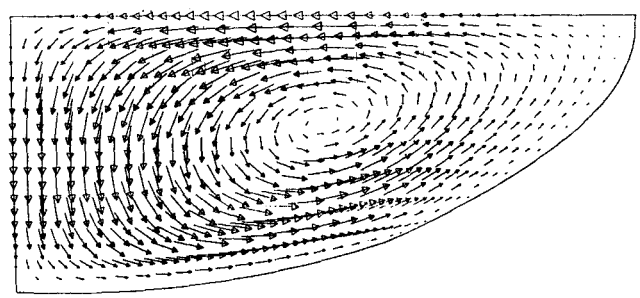

Figure 4. Velocity in weld pool due to Lorentz alone with $I = 100$ *A*, $V_{max} = 20$ mm s$^{-1}$

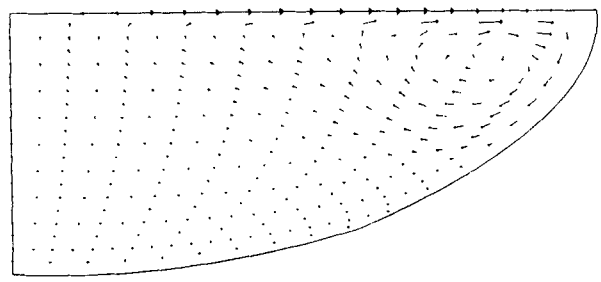

Figure 5. Coarse mesh solution for flow in a fixed axisymmetric domain from an applied quadratic surface velocity profile $V_r = 4V_{max}r(R-r)/R^2$, $V_{max} = 0{\cdot}31\ \mathrm{m\,s^{-1}}$ ($Re = 1000$)

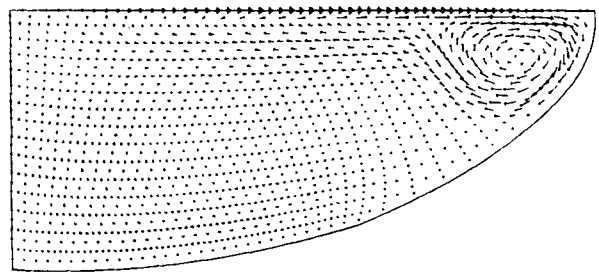

Figure 6. Surface driven flow for axisymmetric weld flow outwardly directed, quadratic profile $V_{max} = 1{\cdot}05\ \mathrm{m\,s^{-1}}$

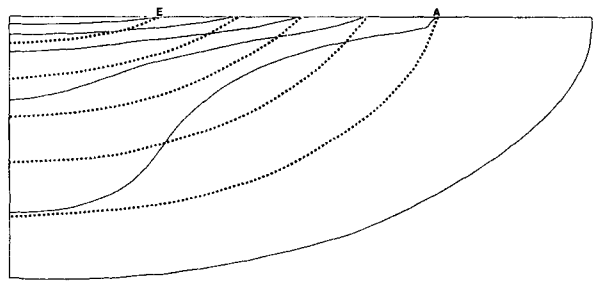


Figure 7. Temperature profiles: $T$ varies from applied surface temperature to melt temperature at the interface $V_{max} = 1{\cdot}0\ \mathrm{m\,s^{-1}}$. Dotted lines are for conduction alone; $T_A = 1646$ K, $T_E = 1832$ K, $\Delta T = 46$ K

those for buoyancy alone since the convective velocity is so small in that instance). Note the large change in the profile closest to the melt boundary—in the strongly convective flow the fluid carries heat out along the surface layer and colder fluid in from the melt wall to the recirculation zone. This supports the argument that shallow welds may be produced due to these convective effects by outward driven flow from surface tension.

As remarked in the introduction, the presence of impurities or certain operating conditions may produce inwardly directed flows. It is instructive to compare the preceding results with those obtained with the same surface velocity field directed inward. The associated convective flow pattern is shown in Figure 8. The convective pattern is much stronger and extends over a large part of the flow domain. The corresponding temperature contours are given in Figure 9 and

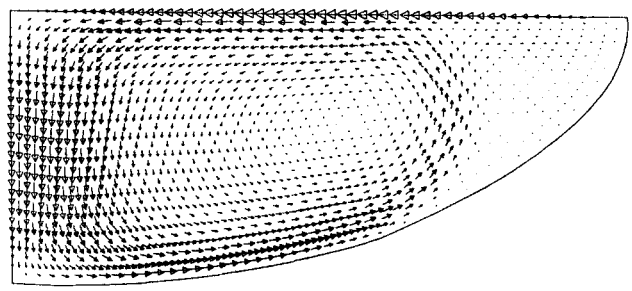

Figure 8. Inwardly driven flow (600 elements); $V_{max} = 1\ m\,s^{-1}$

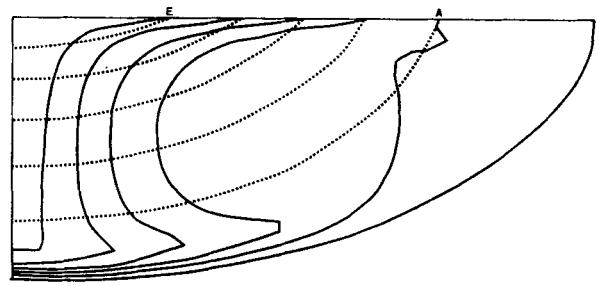


Figure 9. Temperature contours for inwardly directed flow (compare with Figure 7). Dotted contours are for conduction alone; $T_A = 1646$ K, $T_E = 1832$ K, $\Delta T = 46$ K

compared again with those for conduction. The hot surface fluid is carried inward and down through the centre, producing a thermal boundary layer centrally near the melt (crucible) surface of this fixed domain. Such flows will strongly enhance the formation of deep welds.

In experimental studies it has been noted that the free surface of the weld pool may be depressed and that this may be related to the occurrence of 'dry holes' and other 'faults' in the weld. In the next series of numerical studies we compute approximate solutions for a fixed weld pool with a depressed surface. The shape of the depressed surface and pool have been prescribed in advance to approximate the shape considered in Reference 26. The domain and a representative grid for the case of a 1 mm depression are indicated in Figure 10. Our purpose is to examine the influence of surface depression on the flow and heat transport.

For a heated free surface with curvature, the shear due to surface tension depends on both the thermal gradient and the curvature. However, in the present case we prescribe the position of the top surface *a priori*. Hence the computation of the surface tangential shear force driving the flow depends only on the thermal gradient. This implies that the shear stress expression in (9) must be modified to account for the local orientation of the surface in the tangential direction $\hat{\mathbf{s}}$: $\mathbf{T}_s = (\partial\gamma/\partial T)(\partial T/\partial s)\mathbf{v}\cdot\hat{\mathbf{s}}$. The contribution to the integral statement (16) to include the free surface boundary condition now becomes

$$\int_{\partial\Omega_f} \frac{\partial\gamma}{\partial T}\frac{\partial T}{\partial s}\,\hat{\mathbf{s}}\cdot\mathbf{v}\,ds\,. \tag{32}$$

Including this modification in the approximate problem and integrating, we obtain the approximate velocity and temperature solutions.

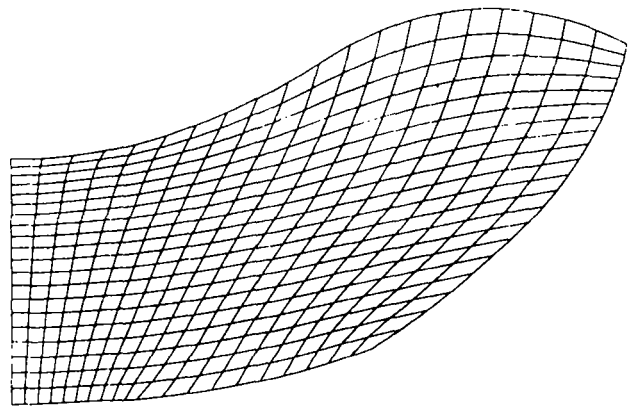

Figure 10. Domain for weld pool with 1 mm depression

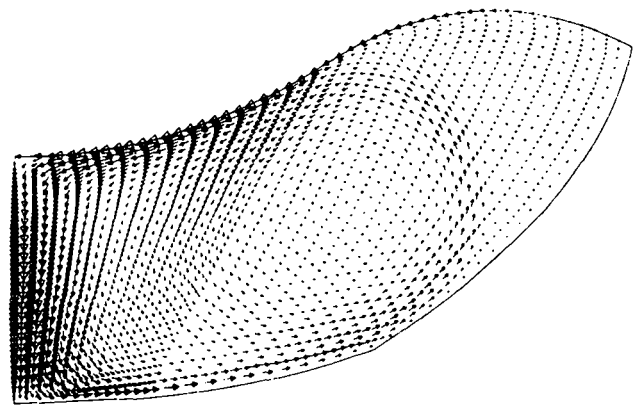

Figure 11. Velocity field for weld pool shape with 1 mm depression; $V_{max} = 1{\cdot}4\ \mathrm{m\,s^{-1}}$ (inward driven flow $d\gamma/dt = 0{\cdot}5 \times 10^{-3}\ \mathrm{N\,m^{-1}\,K^{-1}}$)

As in the previous cases, a cosine 'bump' temperature variation is prescribed as data and scaled incrementally over time to the final temperature value. The velocity field solution is indicated in Figure 11 for the case of inward driven flow at time $t = 0{\cdot}4$ s. Comparing with the flat surface case, we see that the main vortex is translated away from the centreline and is strongest at the 'circle' periphery. There is a relatively 'quiet' zone in the vortex interior and between the vortex and strong downflow at the centreline. A very small secondary flow occurs in the extreme right corner. This flow behaviour is associated with the temperature profiles in Figure 12. The calculation was repeated for a pool with a 2 mm depression, and similar behaviour of the flow fields is observed in Figures 13 and 14 at time $t = 0{\cdot}21$ s. The size of the 'quiet' region at the extreme right is large and contains a small secondary cell. We notice in Figure 14 some irregularities in the temperature profiles near the vortex. These slight oscillations indicate that we are approaching the stability limit of the mesh for this calculation. Calculations attempted on a coarser grid become unstable and diverge as the vortex forms. Finally, in Figures 15 and 16 we show the approximate solution for the pool with a 1 mm surface depression and outward driven flow. A very tight vortex forms at the extreme corner by $t = 0{\cdot}4$ s. There is a large, 'quiet' secondary recirculation cell with flow reversal occurring in a thin layer adjacent to the surface.

A minor point concerning the depressed surface geometry and calculations is of note. Attempts to analyse the problem using two quadratic arcs in a $C^0$ fit to the surface were unsuccessful. The difficulty stems from the fact that this surface approximation is only $C^0$; i.e. the surface slope was

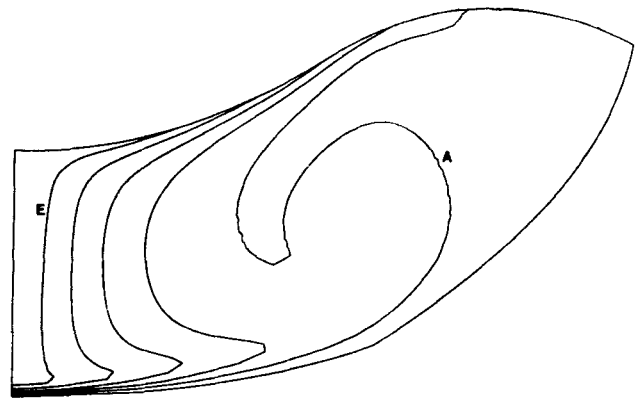


Figure 12. Temperature contours for weld pool shape with 1 mm depression; $T_A = 1733$ K, $T_E = 2267$ K, $\Delta T = 133$ K (inward driven flow $d\gamma/dt = 0{\cdot}5 \times 10^3$ N m$^{-1}$ K$^{-1}$)

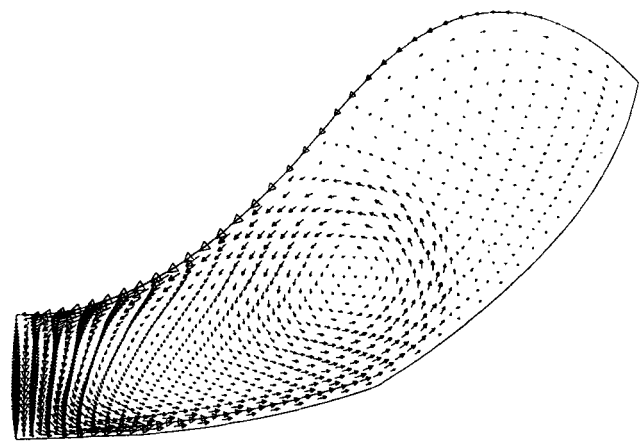

Figure 13. Velocity field for weld pool shape with 2 mm depression; $V_{max} = 1{\cdot}4$ m s$^{-1}$ (inward driven flow $d\gamma/dt = 0{\cdot}5 \times 10^{-3}$ N m$^{-1}$ K$^{-1}$)

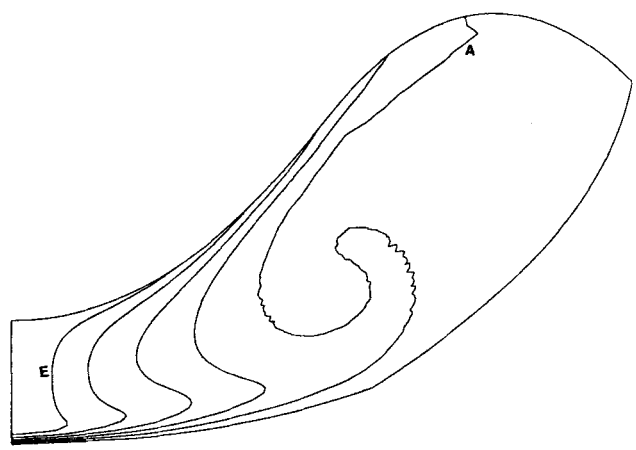


Figure 14. Temperature field for weld pool shape with 2 mm depression; $T_A = 1733$ K, $T_E = 2267$ K, $\Delta T = 133$ K (inward driven flow $d\gamma/dt = 0{\cdot}5 \times 10^{-3}$ N m$^{-1}$ K$^{-1}$)

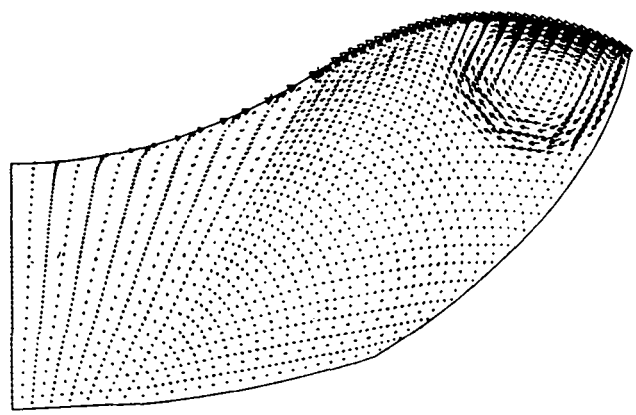

Figure 15. Velocity field for fixed weld pool with 1 mm depression; $V_{max} = 1{\cdot}4\ \mathrm{m\,s^{-1}}$ (outward driven flow $d\gamma/dt = 0{\cdot}56 \times 10^{-3}\ \mathrm{N\,m^{-1}\,K^{-1}}$)

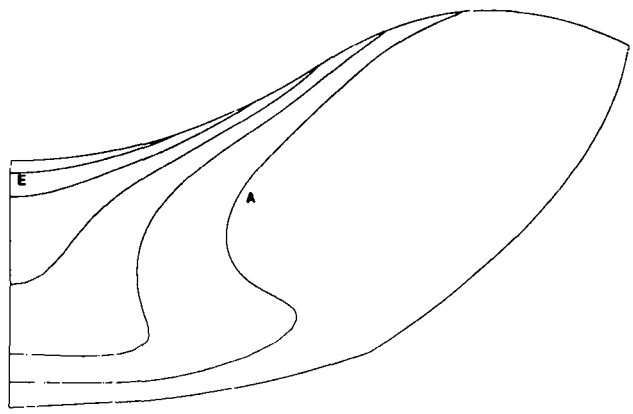


Figire 16. Temperature field for fixed weld pool with 1 mm depression; $T_A = 1733$ K, $T_E = 2267$ K, $\Delta T = 133$ K (outward driven flow $d\gamma/dt = 0{\cdot}56 \times 10^{-3}\ \mathrm{N\,m^{-1}\,K^{-1}}$)

continuous and piecewise smooth but had a small discontinuity at the 'knot'. In computations this discontinuity causes an interaction between the boundary condition of zero normal flow and the shear resulting from surface tension. The usual implementation for zero normal flow is to penalize. However, the discontinuity in slope makes the definition of the normal direction non-unique. Hence penalty contributions influence both normal and tangential directions, thereby constraining the node to have zero velocity. To circumvent this difficulty, we enforced continuity of the slope at this knot for the piecewise quadratics (while preserving the fluid volume of the depressed pool).

Next we consider the moving boundary problem and take as initial data the solution for the fixed weld pool at steady state with inward driven flow. The latent heat condition is now introduced to determine the melt boundary velocity, and the shape of the weld pool plotted at a later time in Figure 17. This is a very demanding test case since the initial data have a strong thermal boundary layer and the phase boundary moves initially with a large velocity $V$. After a short duration, however, as the domain grows, the temperature gradients become less pronounced and growth of the domain slows. The general behaviour of the fluid flow pattern and

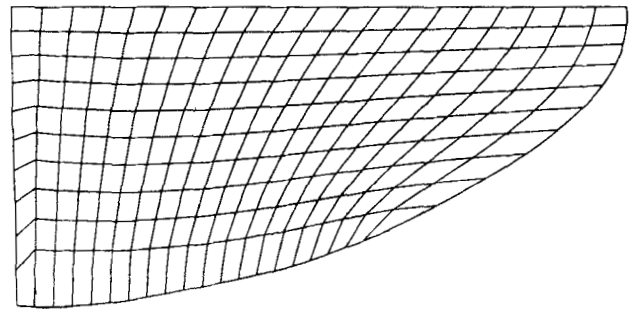

Figure 17. Weld pool mesh after allowing the boundary to melt using velocity and temperature profiles from Figures 8 and 9 as initial data

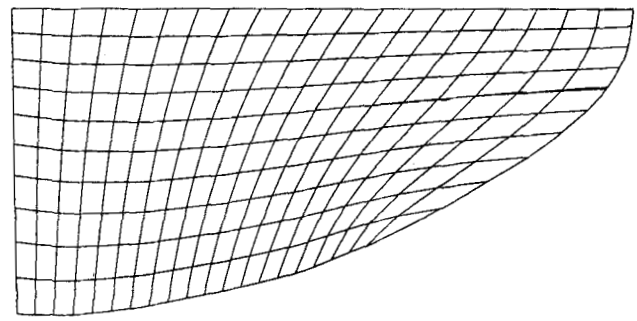

Figure 18. Weld pool mesh after remeshing

temperature field is similar to that shown in Figures 8 and 9. In this case (inwardly directed flow) the weld pool growth is more pronounced toward the centre line because of the larger heat flux there. As indicated previously, after sufficient time the elements adjacent to the phase boundary are elongated. The domain is automatically remeshed as shown in Figure 18.

There are several sensitive issues that arise in the moving mesh and remeshing algorithm. First, the melt boundary should move in accordance with the Stefan condition (3), i.e. the normal to the phase boundary defines the boundary motion. The extreme nodes on the melt boundary also lie on the centreline $r = 0$ and the surface $z = 0$ respectively. Hence these nodes must move with the free surface yet still satisfy these additional requirements. Other nodes on the centreline and free surface should move along these directions proportionally as the extreme nodes move with the phase boundary. These conditions can be readily included as constraints on the boundary node motion for the remeshing algorithm.

A more serious problem arises for nodes on the moving phase boundary. In the analysis presented here, eight-node isoparametric quadrilaterals are employed and the phase boundary is approximated as a $C^0$ piecewise quadratic curve, i.e. the tangential and normal derivatives are discontinuous at the inter-element nodes. This implies that the normal direction is not uniquely defined at the inter-element nodes. In the calculations the normal directions are averaged. In a different context, other mass-conserving projections have been introduced for viscous flow problems,[28, 29] but these are not appropriate here since the motion of the phase boundary is primarily governed by heat transfer, and the momentum equations play a secondary role. Despite averaging, the initially smooth phase boundary becomes 'rippled' due to local inaccuracy in the

velocity (flux) integration and other approximation errors. Accordingly, we introduce a smoothing projection at the remeshing step to filter out high-frequency oscillations in the phase boundary.

A low-order Fourier expansion is introduced to fit the melt boundary:

$$x(s) = \sum_{j=1}^{N} b_j \sin k_j s, \qquad y(s) = \sum_{j=1}^{N} a_j \cos k_j s$$

with $j$ odd. Here $s$ is the arc length along the melt boundary, and $k_j = j\pi/2L$ with $L$ the length of the melt boundary. In the previous example the boundary motion was computed for a few steps using a low value of latent heat to exaggerate the motion. The problem is now computed with a surface heat flux boundary condition $q = (Q/\pi r_j)\exp(-r^2/r_j^2)$ and latent heat $1{\cdot}78 \times 10^9\ \mathrm{J\,m^{-3}}$. The melt boundary is again held fixed from $t = 0$ to $t = 0{\cdot}1$, so the flow and temperature distributions are similar to those in Figure 6 and 7 in the liquid region. An initial weld pool of the same shape as in the preceding studies is assumed with the same initial condition and surface boundary conditions. At the 'remote' bottom $z = -d$ the heat transfer coefficient is $1\ \mathrm{W\,m^{-2}\,K^{-1}}$ and in the far field ($r = R$) the temperature is taken as 300 K. The velocity and temperature distributions are indicated in Figures 19 and 20 at time $t = 0{\cdot}12$ as in the previous calculation. As anticipated, the melt boundary does not move as far as when the solid is non-conducting. The depth is 1·43 mm (159% of the original depth). Here heat is lost by conduction through the solid, so the flux jump is smaller than before and the velocity of the melt boundary reduced accordingly.

## CONCLUDING REMARKS

The problem of coupled viscous flow and heat transfer in a weld pool is analysed using a mixed finite element method for the primitive variable formulation. Important features are the surface tension driven flow (Marangoni effect) and the moving phase boundary. Results computed using good grid resolution on a CRAY computer reveal the detailed structure of the flow circulation regions and layers. The results give much more detail and provide a more comprehensive treatment than those computed previously using finite difference methods and the stream-function–vorticity formulation for fixed weld pool shapes.[15]

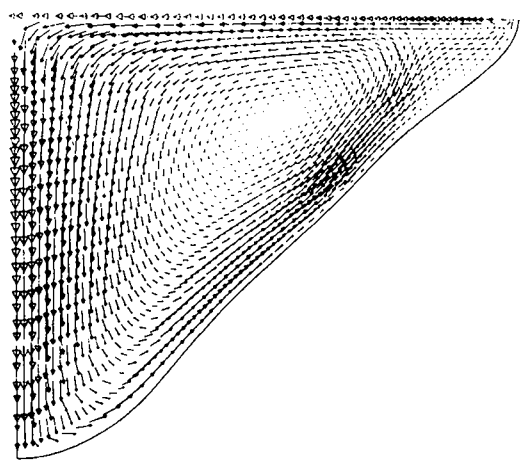

Figure 19. Velocity vectors for a weld pool at $t = 0{\cdot}12$ s, $Q = 1500$ W, $r_q = 4$ mm, $V_{max} = 1{\cdot}25\ \mathrm{m\,s^{-1}}$

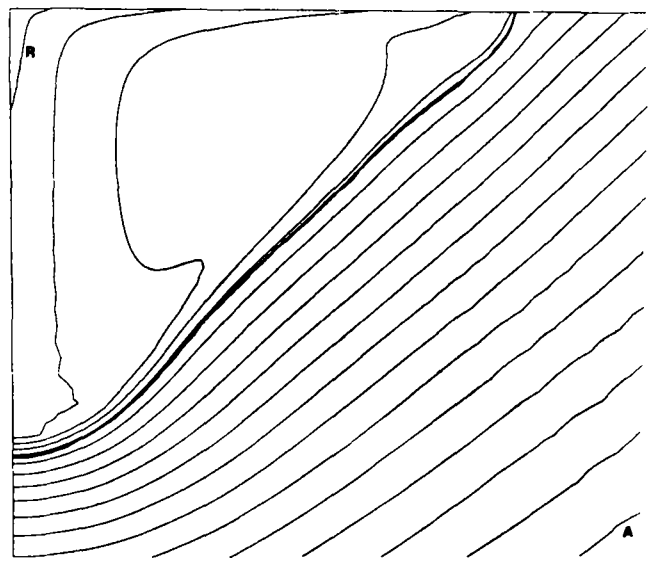


Figure 20. Temperature contours for a weld pool at $t = 0{\cdot}12$ s, $Q = 1500$ W, $r_q = 4$ mm; $T_A = 552$ K, $T_R = 1948$ K, $\Delta T = 82$ K

ACKNOWLEDGEMENT

This research has been supported by the Office of Naval Research Grant N00014-84-K-0426.

REFERENCES

1. A. Oberbeck 'On the thermal conduction of liquids taking into consideration the flow due to differences of temperature' *Ann. Phys. Chem.*, **7**, 271 (1879).
2. J. Boussinesq, *Theorie Analytique de la Chaleur*, 1903.
3. S. Ostrach, 'Motion induced by capillarity', in D. B. Spalding (ed.), *Physiochemical Hydro-dynamics, V. G. Levich Festschrift, Vol. 2*, Advance Publications, Ltd., London, 1977, pp. 571–589.
4. A. Cloot and G. Lebon, 'A nonlinear stability analysis of the Bénard–Marangoni problem', *J. Fluid Mech.*, **145**, 447–469 (1984).
5. C. R. Heiple and J. R. Roper, 'Mechanism for minor element effects on GTA fusion zone geometry', *Welding J.*, **61**, s97–s102 (1982).
6. R. W. Lewis, K, Morgan and P. M. Roberts, 'Determination of thermal stresses in solidification problems', in J. F. T Pittman *et al.* (eds), *Numerical Analysis of Problems*, Wiley, 1984, pp. 405–431.
7. D. K. Gartling, 'Finite element analysis of convective heat transfer problems with change of phase', in K. Morgan *et al.* (eds), *Computers and Fluids*, Pentech Press, London, 1980, pp. 257–284.
8. H. S. Kheshgi and P. Gresho, 'Analysis of electron-beam vaporization of refractory metals', *Electron Beam Melting and Refining State of the Art 1986*, Reno, Nevada, November 1986.
9. P. Gresho, S. Chan, R. L. Lee and C. D. Upson, 'A modified finite element method for solving the time dependent incompressible Navier–Stokes equations, part I: theory, part II: applications' *Int. j. numer. methods fluids*, **4**, 557–598, 619–640 (1984).
10. D. K. Gartling, 'NACHOS—a finite element computer program for incompressible flow problems, Parts I and II', *Sandia Report SAND 77-1333*, April 1978.
11. G. F. Carey and R. McLay, 'Viscous flow and heat transfer with moving phase boundary', *ASME Paper 85-WA/HT-48*, Miami, FL, December 1985.
12. T. J. R. Hughes (ed.), *Finite Element Methods for Convection-Dominated Flows; ASME Monograph 38*, 1980.
13. J. Argyris, J. St. Doltsinis, P. M. Pimenta and H. Wüstenberg, 'Finite element solution of viscous flow problems', in R. H. Gallagher *et al.* (eds), *Finite Elements and Fluids*, Wiley, 1986, pp. 89–114.
14. K. A. Cliffe and K. H. Winters, 'The use of symmetry in Bifurcation problems and its application to the Benard problem', *Report TP.1064*, AERE, Harwell, Oxfordshire, U.K., October 1984.
15. G. M. Oreper and J. Szekeley, 'Heat and fluid flow phenomena in weld pools', *J. Fluid Mech.*, **147**, 53–80 (1984).
16. G. F. Carey and J. T. Oden, *Finite Elements: A Second Course*, Prentice-Hall, Englewood Cliffs., NJ, 1983.

17. D. K. Gartling, 'Finite element analysis of volumetrically heated fluids in an axisymmetric enclosure', in R. H. Gallagher *et al.*, (eds), *Finite Elements in Fluids, Vol. 4*, Wiley, 1982, pp. 233–250.
18. G. F. Carey and J. T. Oden, 'Variational inequalities', in T. J. R. Hughes *et al.* (eds), *New Concepts in Finite Element Analysis; ASME Monograph AMD 44*, 1981, pp. 133–146.
19. R. Glowinski and L. Tremolieres, *Numerical Analysis of Variational Inequalities*, North-Holland, Amsterdam, 1981.
20. R. T. McLay, 'Finite element simulation of coupled fluid flow, heat transfer and magnetic fields with applications to welding', *Dissertation*, Engineering Mechanics, The University of Texas at Austin, August 1988.
21. G. F. Carey and R. T. McLay, 'Local pressure oscillations and boundary treatment for the 8-node quadrilateral', *Int. j. numer. methods fluids*, **6**, 165–172 (1986).
22. A. Mueller and G. F. Carey, 'Continuously deforming finite elements', *Int. j. numer. methods eng.*, **21**, 2099–2126 (1985).
23. K. Miller and R. Miller, 'Moving finite elements: Part I', *SIAM J. Numer. Anal.*, **18**, 1019–1032 (1981).
24. H. P. Wang and R. T. McLay, 'Automatic remeshing scheme for modelling hot forming process', *J. Fluid Eng.*, **108**, 465–469 (1986).
25. M. L. Lin and T. W. Eager, 'Influence of arc pressure on weld pool geometry', *Welding J.*, **64**, 163s–169s (June 1985).
26. R. E. Sundell, W. F. Savage and D. W. Walsh, 'Minor element effects on gas tungsten arc welding penetration', *NSF Report* 86SRD013, General Electric, CRD, Schenectady, NY, 1986.
27. D. R. Atthey, 'A mathematical model for fluid flow in a weld pool at high currents', *J. Fluid Mech.*, **98** (Part 4), 787–801 (1980).
28. W. G. Gray, 'An efficient finite element scheme for two-dimensional surface water computation', in W. Gray *et al.* (eds), *Finite Element in Water Resources*, Pentech Press, 1977, pp. 4.33–4.49.
29. M. S. Engelmann, R. L. Sani and P. M. Gresho, 'Implementation of normal and/or tangential boundary conditions in finite element codes for incompressible fluid flow', *Int. j. numer. methods fluids*, **2**, 225–238 (1982).